



Article

Quantifying Contributions of Local Emissions and Regional Transport to NO_x in Beijing Using TROPOMI Constrained WRF-Chem Simulation

Yizhi Zhu ^{1,2}, Qihou Hu ^{1,*}, Meng Gao ³, Chun Zhao ⁴, Chengxin Zhang ² , Ting Liu ⁴, Yuan Tian ⁵, Liu Yan ⁶, Wenjing Su ⁴, Xinhua Hong ⁷ and Cheng Liu ^{1,2,8,9,10}

- ¹ Key Lab of Environmental Optics & Technology, Anhui Institute of Optics and Fine Mechanics, Chinese Academy of Sciences, Hefei 230031, China; yzz2017@mail.ustc.edu.cn (Y.Z.); chliu81@ustc.edu.cn (C.L.)
- ² Department of Precision Machinery and Precision Instrumentation, University of Science and Technology of China, Hefei 230026, China; zcx2011@mail.ustc.edu.cn
- ³ Department of Geography, Hong Kong Baptist University, Hong Kong 999077, China; mmgao2@hkbu.edu.hk
- ⁴ School of Earth and Space Sciences, University of Science and Technology of China, Hefei 230026, China; chunzhao@ustc.edu.cn (C.Z.); tliu95@mail.ustc.edu.cn (T.L.); swj1993@mail.ustc.edu.cn (W.S.)
- ⁵ Institute of Physical Science and Information Technology, Anhui University, Hefei 230601, China; ytian@ahu.edu.cn
- ⁶ Department of Earth System Science, Tsinghua University, Beijing 100084, China; yanliu17@mails.tsinghua.edu.cn
- ⁷ School of Environmental Science and Optoelectronic Technology, University of Science and Technology of China, Hefei 230026, China; xinhua95@mail.ustc.edu.cn
- ⁸ Anhui Province Key Laboratory of Polar Environment and Global Change, University of Science and Technology of China, Hefei 230026, China
- ⁹ Center for Excellence in Regional Atmospheric Environment, Institute of Urban Environment, Chinese Academy of Sciences, Xiamen 361021, China
- ¹⁰ Key Laboratory of Precision Scientific Instrumentation of Anhui Higher Education Institutes, University of Science and Technology of China, Hefei 230026, China
- * Correspondence: qhhu@aiofm.ac.cn



Citation: Zhu, Y.; Hu, Q.; Gao, M.; Zhao, C.; Zhang, C.; Liu, T.; Tian, Y.; Yan, L.; Su, W.; Hong, X.; et al. Quantifying Contributions of Local Emissions and Regional Transport to NO_x in Beijing Using TROPOMI Constrained WRF-Chem Simulation. *Remote Sens.* **2021**, *13*, 1798. <https://doi.org/10.3390/rs13091798>

Academic Editor:
Constantinos Cartalis

Received: 9 April 2021
Accepted: 1 May 2021
Published: 5 May 2021

Publisher's Note: MDPI stays neutral with regard to jurisdictional claims in published maps and institutional affiliations.



Copyright: © 2021 by the authors. Licensee MDPI, Basel, Switzerland. This article is an open access article distributed under the terms and conditions of the Creative Commons Attribution (CC BY) license (<https://creativecommons.org/licenses/by/4.0/>).

Abstract: Air quality is strongly influenced by both local emissions and regional transport. Atmospheric chemical transport models can distinguish between emissions and regional transport sources in air pollutant concentrations. However, quantifying model inventories is challenging due to emission changes caused by the recent strict control measures taken by the Chinese government. In this study, we use NO₂ column observations from the Tropospheric Monitoring Instrument to retrieve top-down nitrogen oxide (NO_x) emissions and quantify the contributions of local emissions and regional transport to NO_x in Beijing (BJ), from 1 November 2018 to 28 February 2019 (W_2018) and 1 November 2019 to 29 February 2020 (W_2019). In W_2018 and W_2019, the BJ bottom-up NO_x emissions from the multi-resolution emission inventory for China in 2017 were overestimated by 11.8% and 40.5%, respectively, and the input of NO_x from other cities to BJ was overestimated by 10.9% and 51.6%, respectively. The simulation using our adjusted inventory exhibited a much higher spatial agreement (slope = 1.0, R² = 0.79) and reduced a mean relative error by 45% compared to those of bottom-up NO_x emissions. The top-down inventory indicated that (1) city boundary transport contributes approximately 40% of the NO_x concentration in BJ; (2) in W_2019, NO_x emissions and transport in BJ decreased by 20.4% and 17.2%, respectively, compared to those of W_2018; (3) in W_2019, NO_x influx substantially decreased (−699 g/s) in BJ compared to that of W_2018 despite negative meteorological conditions that should have increased NO_x influx by +503 g/s. Overall, the contribution of intercity input to NO_x in BJ has declined with decreasing emissions in the surrounding cities due to regional cooperative control measures, and the role of local emissions in BJ NO_x levels was more prominent. Our findings indicate that local emissions may play vital roles in regional center city air quality.

Keywords: tropospheric monitoring instrument; weather research and forecasting with coupled chemistry; top-down nitrogen oxide emissions; transport; meteorology

1. Introduction

In the past decade, haze in China has been frequently reported at unprecedented $PM_{2.5}$ concentrations during the autumn and winter, particularly in the North China Plain (NCP). Nitrogen oxides (NO_x ; $NO + NO_2$), which are primarily discharged by anthropogenic activities, such as fossil fuel combustion [1], are a group of reactive trace gases. NO_x is not only toxic to human health, but also play a key role in the formation of secondary aerosol and tropospheric ozone [2]. Therefore, NO_x is crucial atmospheric air pollutants.

A series of strict emissions reduction measures was implemented in China beginning in September 2013 [3]. In the past seven years, substantial manpower and material resources have been invested to improve air quality, and major measures have been taken for the atmosphere and ecosystem. To evaluate the effectiveness of air pollution control measures, an accurate and high spatiotemporal resolution of NO_2 distribution must be obtained [4–6]. Most previous studies have primarily used satellite observations, regional air quality model simulations, or ground-based observations to obtain the trace gas distribution [7–11]. Compared with these methods, the NO_2 concentration produced by models (Global 3-D model of atmospheric chemistry driven by meteorological input from the Goddard Earth Observing System (GEOS-Chem) [12], Community Multiscale Air Quality (CMAQ) model, Comprehensive Air Quality Model with Extensions (CAMx)) exhibits a higher spatiotemporal resolution in both the horizontal and vertical directions. Thus, timely NO_x emission data are necessary.

A top-down inversion using satellite retrieval products of tropospheric vertical column densities (VCDs) of NO_2 is widely used to estimate NO_x emissions. This method accounts for the nonlinear effects of horizontal transport, chemical loss, and deposition. Previous studies have estimated NO_x emissions from various regions worldwide, including North America, Asia, the Middle East, and Europe [13–17]. This inversion has also been used to produce and validate NO_x emission estimations from sources such as soil, lightning, power plants, aircraft, marine vessels, and urban centers [8,18–21].

The NO_x concentration distribution is not only related to regional NO_x emissions but also linked with the regional transport of NO_x . Several quantitative and qualitative approaches have been applied to evaluate the regional transport of emissions and its effect on local air quality [22–25]. The backward trajectory based on meteorology analysis has been used to qualitatively identify and describe the major transport direction and pathway of a target city [23,26–28]. Additionally, certain studies have used meteorological models or have combined meteorology and air quality observations to determine the relative importance of different source regions as a semi-qualitative assessment. Such studies include footprint analysis [29,30], the potential source contribution function analysis [31–33], and flux calculation [34]. Recently, regional transport studies have mostly been based on the chemical transport model [35] to sufficiently consider both the physical and chemical processes. For example, [36] found three primary transport pathways inside the Beijing–Tianjin–Hebei (BTH) region, i.e., the southwest, southeast, and anticlockwise pathway, with the Community Multiscale Air Quality and Integrated Source Apportionment Model (CMAQ-ISAM) [37] quantified the contribution of pollutant transport via $PM_{2.5}$ concentrations in 13 cities in the BTH region using the CMAQ-ISAM model. These findings have noted the necessity of a regional joint-control strategy. However, these studies are based on inventories relying on indirect information that is often outdated or incomplete, which is insufficient to support the development of a comprehensive joint-control strategy.

Herein, we combined the Tropospheric Monitoring Instrument (TROPOMI) observations and Weather Research and Forecasting with coupled chemistry (WRF-Chem) simulations to obtain accurate NO_x emissions for the NCP region (covering $33^\circ N$ – $43^\circ N$, $109^\circ E$ – $123^\circ E$). We then identify the sources and sinks of NO_x in NCP based on the regional transport flux. Finally, we quantify the contributions of NO_x local emissions and regional transport to NO_x concentrations, distinguishing the roles of meteorology and emissions to the city-

boundary transport flux, thus helping the government implement emissions reduction policies at the city level. The remainder of this paper is organized as follows. Section 2 provides detailed information about the model configuration, TROPOMI NO₂ retrieval, top-down NO_x emissions inversion, and transport flux calculation. The top-down NO_x inventory evaluation, relative contribution of NO_x emissions and transport flux to NO_x concentration, and role of emissions control and meteorology analysis are presented in Section 3. Section 4 presents the discussion. Finally, conclusions are present in Section 5.

2. Materials and Methods

2.1. Model Description and Configuration

The meteorological parameters and NO_x concentration were provided by WRF-Chem version 4.0. This modeling system runs in two parts: the dynamic and chemical modules. The WRF model, which is a mesoscale numerical weather prediction system designed for meteorological research and numerical weather forecasting, is used as the dynamic module. A detailed description of the WRF model is available at the WRF website (<http://www.wrf-model.org/index.php>, last access: 15 March 2020). In addition to dynamical calculations, the chemical module is fully coupled with the WRF model online [38]. A detailed illustration of the chemical composition is provided by Grell et al. [39]. In this work, the simulation domain covered East China and its surrounding area, with a center point of 38.0°N, 115.6°E. The model's horizontal resolution was selected to be 20 × 20 km², with 89 × 79 grids (there are 89 grids in the east-west direction and 79 grids in the north-south direction). From the ground level to the top pressure of 10 hPa, there were 44 vertical sigma layers for all grids. The initial meteorological fields and boundary conditions were from the 6-h final operational global analysis (FNL) data. The data were provided by the National Centers for Environmental Prediction (NCEP), and it exhibited a 1° × 1° spatial resolution. Furthermore, the NCEP Administrative Data Processing (ADP) Global Surface Observational Weather Data (ds461.0) and Upper Air Observational Weather Data (ds351.0) with 6-hourly temporal resolution were used to accurately reproduce the meteorology. The physical and chemical parameterization schemes adopted in this study are detailed in Table 1. Further configuration options of the model can be found in our previous study [40]. Table 2 demonstrates that the simulated wind fields are reproducible in comparison with those of the National Office for Oceanic and Atmospheric Administration (NOAA) observations (<https://www.ncdc.noaa.gov/>, last access: 25 June 2020).

The Carbon-Bond Mechanism version Z photochemical mechanism combined with the Model for Simulating Aerosol Interactions and Chemistry was used to simulate the chemical process in the atmosphere. The anthropogenic emissions were taken from the multi-resolution emission inventory for China in 2017 (MEIC-2017; <http://www.meicmodel.org/>, last access: 17 March 2020) [41,42]. The biogenic emissions were calculated online using the Model of Emissions of Gases and Aerosols from Nature embedded in the WRF-Chem model. The near-real-time fire emissions from the fire inventory of NCAR based on Moderate Resolution Imaging Spectroradiometer rapid response fire counts (<https://www.acom.ucar.edu/acresp/forecast/fire-emissions.shtml>, last access: 18 March 2020).

Table 1. Model configuration options.

Schemes	Description
Microphysics	Purdue Lin Scheme [43]
Longwave radiation	Rapid radiative transfer model (RRTMG) scheme [44]
Shortwave radiation	RRTMG scheme
Cumulus parameterization	Grell–Freitas Ensemble Scheme [45]
Land surface	Unified Noah Land Surface Model [46]
Planetary boundary layer	Yonsei University scheme [47]
Chemical mechanism	Carbon-Bond Mechanism version Z
Photolysis scheme	Fast-J photolysis

Table 2. Comparison of wind field from WRF simulation and NOAA observations.

Meteorological Parameter	Statistic	Unit	Mean	Standard Deviation
Wind Speed	MeanOBS	(m/s)	4.32	
	MeanPRD	(m/s)	3.97	
	Bias	(m/s)	0.37	$\leq \pm 0.5$
	GrossError	(m/s)	1.13	< 2
	Root mean square error (RMSE)	(m/s)	1.86	< 2
Wind Direction	MeanOBS	($^{\circ}$)	337	
	MeanPRD	($^{\circ}$)	288	
	Bias	($^{\circ}$)	5.25	≤ 10
	GrossError	($^{\circ}$)	48.32	$\leq \pm 30$
	RMSE	($^{\circ}$)	79.81	

2.2. TROPOMI Satellite Observation

TROPOMI is a passive trace gas spectrometer aboard the Sentinel-5 Precursor satellite, which was launched on 13 October 2017. TROPOMI measures the reflected sunlight of the atmosphere with spectral bands in 270–500 nm (ultraviolet–visible) 675–775 nm (near-infrared), and 2305–2385 nm (short-wave infrared) at a moderate resolution (0.25 nm to 0.6 nm), enabling daily global coverage with a spatial resolution of 7 km \times 3.5 km at an exact nadir point [48,49]. In this work, the TROPOMI NO₂ product typically followed the satellite trace gas retrieval algorithms by USTC (University of Science and Technology of China) [50]. During NO₂ slant column density retrieval, the wavelength range of 405–465 nm was selected for the NO₂ spectral fit performed with the QDOAS software package [51]. The QDOAS configurations follow the suggestions in the QA4ECV NO₂ project [52]. For NO₂ air mass factor (AMF) calculations, the Vector Linearized Discrete Ordinate Radiative-Transfer version 2.7 model [53] was used to calculate the stratospheric and tropospheric NO₂ AMF pixel by pixel. During the RTM calculations, a priori NO₂ profile with a high-resolution of 20 km \times 20 km was taken from the monthly WRF-Chem simulations. Other information, such as cloud top pressure, cloud fraction, and surface albedo, was obtained from the operational TROPOMI cloud dataset [54]. To separate the stratospheric contribution from the total NO₂ VCDs, a modified reference sector method, i.e., the STREAM algorithm [55], was applied. For the final tropospheric NO₂ VCDs, we utilized a novel P-spline method to re-grid the NO₂ VCDs to the Level-3 product at a resolution of 0.2 $^{\circ}$ \times 0.2 $^{\circ}$ [56]. TROPOMI data were considered cloud-contaminated and filtered out by the re-gridding algorithm when the cloud radiance fraction was greater than 50% [57,58].

2.3. TROPOMI-Derived Top-Down NO_x Emissions

TROPOMI-detected NO₂ columns are sensitive to NO_x emissions at the surface and are influenced by the NO_x lifetime within the plumes. Previous studies [18,59,60] have confirmed that there is a non-linear relationship between changes in surface NO_x emissions and changes in tropospheric NO₂ columns. This is because an increase in the NO_x concentration may promote or inhibit oxidation losses [11]. In the monthly assimilated inversion, we referenced the framework by [61]. The following four steps were followed. (1) Two simulations were performed, one with a priori emissions MEIC-2017 (E_{meic}) and another with anthropogenic NO_x emissions, which increased by 20%. (2) The dimensionless scaling factor β , which reflects the sensitivity of NO₂ VCDs to local NO_x emissions via NO_x-OH chemistry (indicated by Formula (1)), was calculated. (3) Top-down NO_x emissions ($E_{top-down}$) were estimated with the modeled sensitivity β to scale the a priori emissions (indicated by Equation (2)). (4) The monthly regional NO_x distribution was modeled with WRF-chem to combine the top-down emissions.

$$\beta = \frac{\Delta E / E_{meic}}{\Delta C / C_{meic}} \quad (1)$$

$$E_{top-down} = E_{meic} \left(1 + \beta \frac{C_{tropomi} - C_{meic}}{C_{meic}} \right) \quad (2)$$

where ΔE is the change in anthropogenic NO_x emissions in E_{meic} , which increased by 20%; C_{meic} is the simulated NO_2 columns with E_{meic} ; ΔC is the change in the monthly average tropospheric-simulated NO_2 VCDs after perturbing E_{meic} anthropogenic NO_x emissions by +20%. $C_{tropomi}$ is the monthly average tropospheric VCDs based on WRF-Chem NO_2 vertical profile with E_{meic} . Equation (2) in this work is a simplified calculation from [61]. In our study, the difference of top-down NO_x emissions from Equation (2) is ~0.2% lower than that calculated by [61].

2.4. Horizontal Transportation Flux

To further investigate the source and sink centers of air pollution in the NCP region, the spatial distribution of the transport flux was calculated as follows:

Step 1: Calculate the average wind.

The weight coefficient was derived from the vertical distribution of NO_2 under the height of the tropopause layer in each grid. A high NO_2 concentration corresponds to a large coefficient. The average wind is equal to the sum of the wind of each layer multiplied by the weight coefficient of the corresponding height.

Step 2: Calculate the horizontal transport flux of grid A (i, j) [62].

$$\text{East-west direction } flux_{a(i,j)} = C_{(i+1,j)} * U_{(i+1,j)} - C_{(i-1,j)} * U_{(i,j)} \quad (3)$$

$$\text{North-south direction } flux_{b(i,j)} = C_{(i,j+1)} * V_{(i,j+1)} - C_{(i,j-1)} * V_{(i,j)} \quad (4)$$

$$\text{Horizontal net flux } flux_{net(i,j)} = flux_{a(i,j)} + flux_{b(i,j)} \quad (5)$$

Equations (3) and (4) provide the basic equations to calculate the transport flux of each grid in the region. Where C is the tropospheric NO_2 column from the WRF-Chem NO_2 simulation. U and V represent the winds in the east-west and north-south directions, respectively. Easterly and northerly are both positive. Equation (5) quantifies the net flux of air pollutants in each grid. A positive net-flux represents the grid outputting NO_2 to its surrounding four grids. By contrast, negative values indicate that the four surrounding grids input NO_2 into the grid.

2.5. Ancillary Data

In-situ measurements for NO_2 analysis were provided by the operational stations of the China Environmental Observation Network operated by the China National Environmental Monitoring Centre (CNEMC; <http://www.cnemc.cn/en/>, last access: 28 June 2020). The 0–23-h concentrations of these measurements spanning from November 2018 to February 2019 and from November 2019 to February 2020 were used in this study. FNL data were obtained from NCEP FNL Operational Model Global Tropospheric Analyses (<https://rda.ucar.edu/datasets/ds083.2/index.html>, last access: 15 March 2020). NCAR archive ds351.0 data were downloaded from NCEP ADP Global Upper Air Observational Weather Data Centre (<https://rda.ucar.edu/datasets/ds351.0/index.html>, last access: 15 March 2020)

3. Results and Discussion

3.1. Top-down Emissions Evaluation

Wintertime air pollution is extremely severe in northern Chinese cities. In February 2017, the Ministry of Environmental Protection in China released the Air Pollution Prevention and Control Work Plan for BTH and its neighboring regions, which referred to the cities that transmit air pollution as “2 + 26” cities (represented by triangles in Figure 1) for the first time. The “2 + 26” cities represent 28 NO_x polluted cities in the Beijing-Tianjin-Hebei and surrounding region, including 2 cities with significant NO_x pollution (Beijing (BJ) and Tianjin (TJ)) and 26 cities (the rest of the cities) with high NO_x concentrations. Since the implementation of air emissions control in the “2 + 26” cities, the concentration of air pollu-

tion has been significantly reduced, and the air quality has been greatly improved. Monthly top-down NO_x emissions were derived using the method described in Section 2. Figure 1 displays the spatial distribution of monthly averaged MEIC-2017 and top-down surface NO_x emissions. “2 + 26” cities dominated in high NO_x emissions. Figure 2 illustrates the regional emission differences. As exhibited in Figure 2a,b, the top-down NO_x emissions in the south of BJ, southeast of Hebei province, northwest of Shandong province, and northern of Henan province were significantly reduced by 25–58% when compared to those of MEIC-2017. By contrast, NO_x emissions in Taiyuan (TY) and Tangshan (TS) slightly increased. This phenomenon can also be observed in Figure S2a–f, except for January 2020. In February 2020, NO₂ VCDs in the south of TY simulated from top-down W_2019 are slightly higher than that simulated from MEIC-2017 (Figure S2h). However, NO₂ VCDs in the south of TY simulated from top-down W_2019 is slightly lower than that simulated from top-down W_2018 (Figure S2i) during February 2020. This means that NO_x emissions in the south of TY during February 2020 are higher than that in the same period of 2017, but lower than that in the same period of 2019. Figure 2c displays the difference between the top-down inventories in W_2018 and W_2019. NO_x emissions in all “2 + 26” cities significantly decreased. The monthly variation analysis (Figure S2i–l) shows that NO_x emissions in the south of BJ and southeast of TJ and Langfang (LF) slightly increased, while NO_x emissions in the other cities decreased in November 2019 compared to those in November 2018, particularly in central Shanxi. In December 2019, most cities in the southeast of Taihang Mountain exhibited significant NO_x emission reductions compared to those in December 2018, while NO_x emissions in central Shanxi province and Tangshan increased. In January 2020, NO_x emissions across the entire study area exhibited a pronounced decreasing trend compared to those in January 2019; and the NO₂ concentration in the BTH demonstrated a reduction of approximately 50% compared with that in January 2019. This result may be attributed to the lockdown policy during the outbreak of the COVID-19 pandemic. Additionally, it may have also resulted from the influence of the Spring Festival holiday.

Figure 3 compares the monthly averaged NO₂ tropospheric VCDs simulated from MEIC-2017, top-down NO_x emissions, and their differences. Figure 3a illustrates the monthly average distribution of tropospheric NO₂ VCDs in W_2018, which was simulated using the MEIC-2017 inventory, and Figure 3b is the same as Figure 3a, except that it uses the top-down W_2018 NO_x inventory, which was retrieved from the TROPOMI NO₂ concentration during W_2018. Both Figures 3a and 3b exhibit peak NO₂ in BJ, TJ, TS, and certain cities in southeast of the Taihang mountains. Figure 3c displays the monthly averaged distribution of tropospheric NO₂ in W_2019, which uses the same inventory as that in Figure 3a. The role of meteorological conditions can be understood based on the difference between Figures 3a and 3c. The overall meteorology changes between W_2018 and W_2019 slightly influenced the NO₂ VCDs and their spatial distribution. Figure 3d is the same as Figure 3c, except that it uses the top-down W_2018 inventory, the VCD distribution of which is similar to that of Figure 3b. Figure 3e is the same as Figure 3c, except that it uses the top-down W_2019 inventory, which was retrieved from the TROPOMI NO₂ observations during W_2019. Figure 3f indicates the difference between Figures 3a and 3b, reflecting the changes in the tropospheric NO₂ VCDs during W_2018 when using the calibration inventory compared to that when using MEIC-2017. In most cities, the NO₂ concentration dropped significantly, while strong (18–32%) NO₂ concentration increases occurred in the center of Shanxi province and TS after NO_x emission adjustments during W_2018. In February 2019, the simulated NO₂ VCDs using top-down W_2018 inventory was significantly lower than that using MEIC-2017 in the study area (Figure S3a–d,i–l). This result was due to reduced NO_x emissions over the Spring Festival holiday. Figure 3g indicates the difference between Figures 3c and 3d, reflecting the changes in the tropospheric NO₂ VCDs during W_2019 when using the top-down W_2018 inventory compared to that when using MEIC-2017. The decline in NO₂ VCDs in Figure 3g is more pronounced than that in Figure 3f, which was caused by the unfavorable meteorological condition

during W_2019 compared to that in W_2018. Figure 3h indicates the differences between Figures 3c and 3e, reflecting the changes in the tropospheric NO₂ VCDs during W_2019 when using the calibration inventory compared to that when using MEIC-2017. The NO₂ VCDs simulated from the top-down-W_2019 are much lower than those from MEIC-2017, especially in January and February 2020. The NO₂ concentration in the BTH region particularly decreased. The decline in NO₂ VCDs in Figure 3h is more pronounced than that in Figure 3f, which was caused by the significantly decreased NO_x emissions during W_2019. This substantial drop in the NO₂ concentration was due to a combination of strict emission controls and the COVID-19 lockdown.

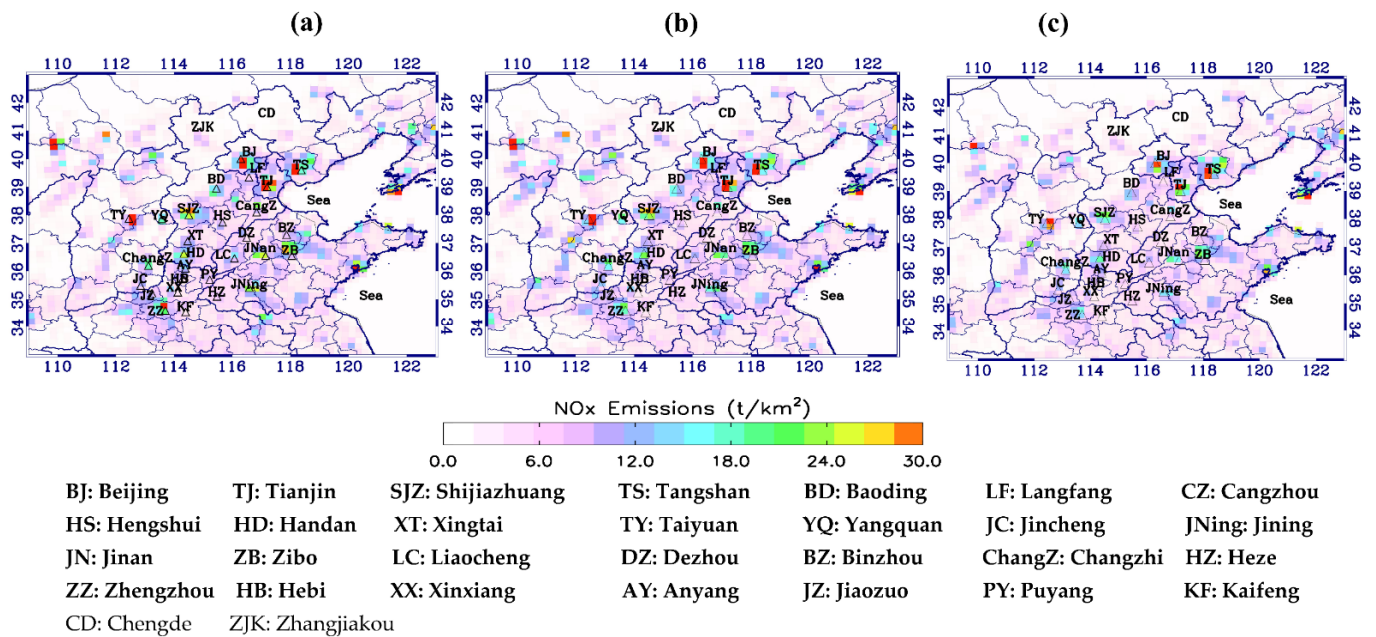


Figure 1. Four-month averaged nitrogen oxide (NO_x) emissions for (a) the multi-resolution emission inventory for China in 2017 (MEIC-2017), (b) top-down 1 November 2018 to 28 February 2019 (W_2018), and (c) top-down 1 November 2019 to 29 February 2020 (W_2019). (a) is four-month average for January, February, November, and December. ‘Four-month averaged’ in this paper refers to average of four months as indicated above, while the supplementary material is average of each month.

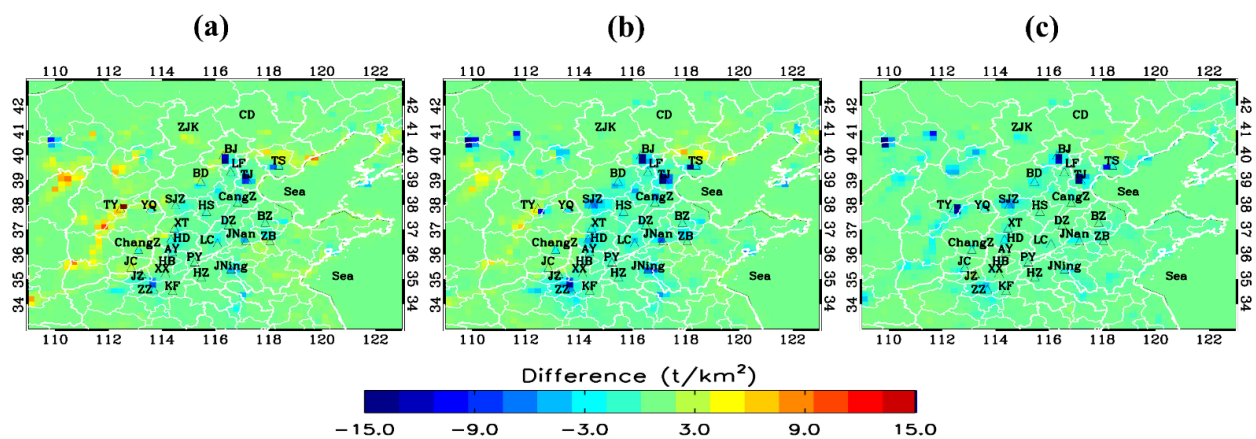


Figure 2. Differences in four-month averaged NO_x emissions between MEIC-2017 and top-down NO_x emissions; (a) indicates top-down W_2018 minus MEIC-2017; (b) indicates top-down W_2019 minus MEIC-2017. (c) Change in surface NO_x emissions between top-down W_2018 and top-down W_2019 (top-down W_2019 minus top-down W_2018).

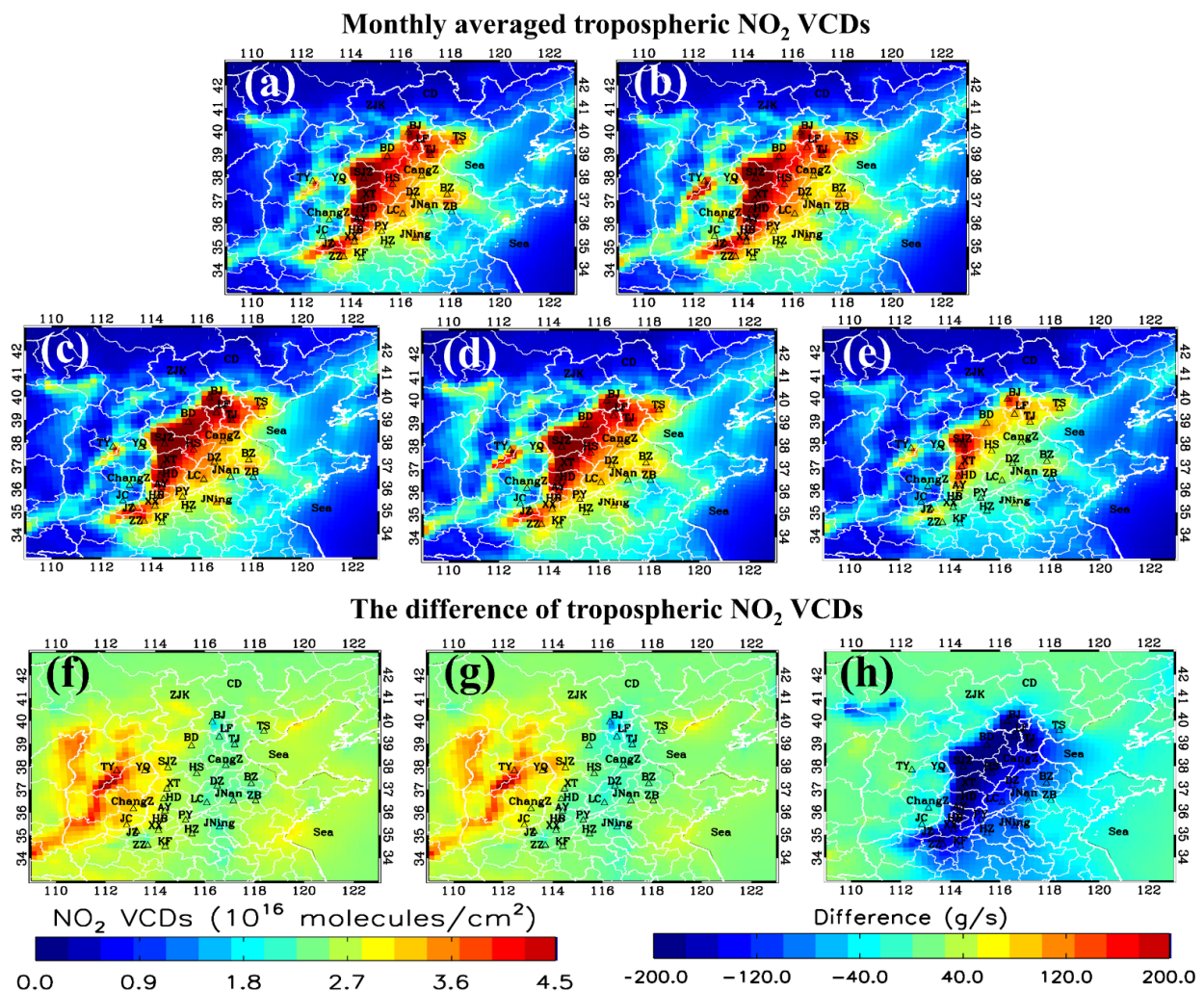


Figure 3. Four-month averaged tropospheric NO₂ VCDs simulated from MEIC-2017, top-down NO_x emissions, and their differences. (a) Simulated NO₂ VCDs in W_2018 with MEIC-2017 inventory. (b) Same as (a) except with top-down W_2018 inventory. (c) Simulated NO₂ VCDs in W_2019 with MEIC-2017 inventory. (d) Same as (c) except with top-down W_2018 inventory. (e) Same as (c) except with top-down W_2019 inventory. (f) Difference between (a) and (b) ((b) minus (a)). (g) Difference between (c) and (d) ((d) minus (c)). (h) Difference between (c) and (e) ((e) minus (c)).

Figure 4 illustrates the simulation with optimized NO_x emissions and removing the model's systematic bias with respect to the hourly surface in-situ NO₂ concentration, leading to an improved spatial agreement (slope = 1.0, $R^2 = 0.79$) and reducing the mean relative error by 45%. Our findings demonstrate that air quality model simulations combined with satellite observations can be used to adjust surface NO_x emissions before more rigorous bottom-up emissions inventories are released.

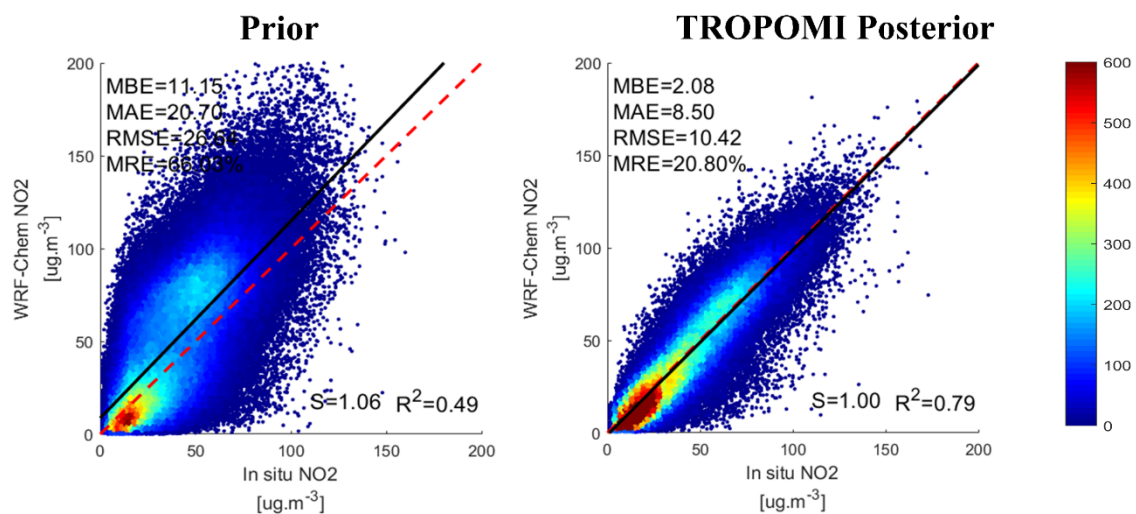


Figure 4. Correlation analysis of in-situ surface NO₂ concentrations (from China National Environmental Monitoring Centre) and simulated NO₂ using prior (MEIC-2017) and TROPOMI posterior (top-down W₂₀₁₈ and W₂₀₁₉) inventories. MBE: Mean Bias Error, MAE: Mean Absolute Error, RMSE: Root Mean Squared Error, MRE: Mean Relative Error.

3.2. Regional Transport Flux

Studies have been extensively performed to investigate the impact of regional transport on BJ airborne species [63–65]. Figure 5a–h display the NO₂ regional transport fluxes and their differences calculated using formulas (3–5), which correspond to Figure 3a–h, respectively. During the two periods, TS, TJ, and cities in southeast of Taihang mountain (Baoding (BD), Shijiazhuang, Xingtai, Handan, Anyang, and Hebi) were significant NO₂ sources when using MEIC-2017 (Figure 5a,c), and they were lesser sources when using top-down NO_x emissions (Figure 5f–h). These results indicate great achievements in emission reductions due to the implementation of strict emissions control measures. By contrast, cities in central Shanxi province exhibited more NO_x emissions when using top-down NO_x emissions than when using MEIC-2017 emissions. This result means that TY and its surrounding cities to the north need to strengthen their emission reduction management.

A city that exhibits a high NO₂ concentration does not necessarily severely emit NO_x. Moreover, the wind field makes NO₂ flow into and accumulate in that city, which also leads to heavy NO₂ pollution. For example, BJ exhibits a high NO₂ concentration during the two periods; however, it is a NO_x sink. In addition, the regional distribution of sources and sinks agrees with that of the NO_x emissions. Satellite observations can be used to qualitatively analyze source distribution and strength without updating the bottom-up emissions. The distribution of sources in the regional transport flux is affected by the wind field. When the wind speed is low, and the wind direction frequently changes, the transport flux agreement with bottom-up NO_x emissions improves. These findings are considerably important for implementing air quality control measures during special events.

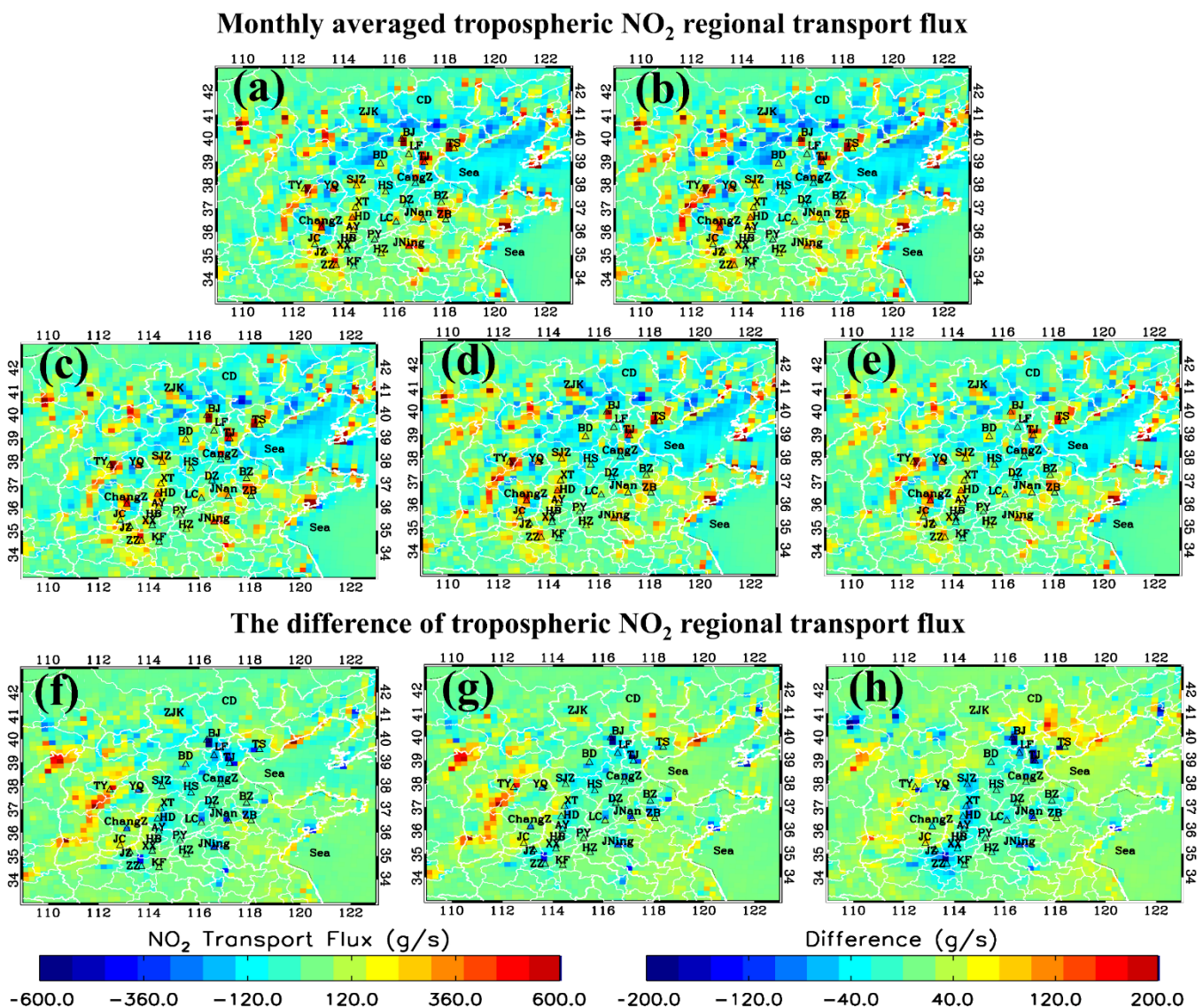


Figure 5. Four-month averaged tropospheric NO₂ regional transport flux (region with positive value indicates source of NO₂, and negative value indicates sink of NO₂) derived from MEIC-2017, top-down NO_x emissions, and their differences. (a) Calculated NO₂ flux in W_2018 with MEIC-2017 inventory. (b) Same as (a) except with top-down W_2018 inventory. (c) Calculated NO₂ flux in W_2019 with MEIC-2017 inventory. (d) Same as (c) except with top-down W_2018 inventory. (e) Same as (c) except with top-down W_2019 inventory. (f) Difference between (a) and (b) ((b) minus (a)). (g) Difference between (c) and (d) ((d) minus (c)). (h) Difference between (c) and (e) ((e) minus (c)).

3.3. Assessment of City Boundary Transport Around BJ

To determine the effectiveness of emissions control measures on each city level, the relative contributions of local NO_x emissions and city boundary transport fluxes must be quantified. Figure 6 represents the NO_x transport fluxes surrounding BJ, the calculation method of which is derived from [35]. BJ is a large NO_x sink in both periods. Zhangjiakou (ZJK) and BD, which are upwind of BJ, input NO_x into BJ (the NO_x transported through the outer boundary is a mixture of different sources and does not solely stem from the neighboring cities). BJ simultaneously exports NO_x to the downwind cities, such as Chengde (CD), TJ, and LF. Figure 6a,c demonstrate the transport fluxes between BJ and its surrounding 5 cities during W_2018 and W_2019, which are simulated using MIEC-2017 (same MEIC-2017 NO_x emissions but different meteorology). In that case, the difference (Figure 6c minus Figure 6a) in the boundary transport flux of BJ is due to the meteorology change between the two periods. In W_2019, BJ exhibits enhanced NO_x input from

surrounding cities by 597 g/s (13.2%) compared to that of W_2018. The unfavorable meteorology in W_2019 can account for the 13.2% NO_x concentration enhancement. Figure 6b exhibits the cities boundary transport flux between BJ and its surrounding cities during W_2018, which is the same as Figure 6a except that it uses the top-down W_2018 inventory. Figure 6d is the same as Figure 6c except that it uses the top-down W_2018 inventory. Comparing Figures 6d and 6b, i.e., the weather of W_2019 compared to that of W_2018, demonstrated an increase in the BJ input flux by 503 g/s (12.4%), which also reflects the adverse meteorological conditions in W_2019 causing NO_x concentration enhancement. Figure 6e is the same as Figure 6d, except that the top-down W_2019 inventory was used. Comparing Figures 6e and 6d, the NO_x emissions in top-down W_2019 compared to that in the top-down W_2018, for the BJ input were reduced by 1202 g/s (26.3%), which also reflects the favorable emissions control in W_2019 for NO_x concentration reduction. Comparing Figures 6b and 6a, the boundary transport flux simulated using MEIC-2017 overestimates the NO₂ inflow flux in BJ by 443 g/s (10.9%) during W_2018. Comparing Figures 6e and 6c demonstrates that the boundary transport flux simulated and calculated using MEIC-2017 overestimates the NO₂ inflow flux in BJ by 1379 g/s (51.6%) during W_2019. Comparing Figures 6e and 6b reflects that the input of NO₂ from cities surrounding BJ exhibits a decrease in NO_x emissions of 699 g/s (17.2%) from W_2018 to W_2019. This result is caused by the co-effects of meteorology and emissions changes. The favorable contribution of the emission reduction policy is 26.3%, while the unfavorable contribution of weather is approximately 13%.

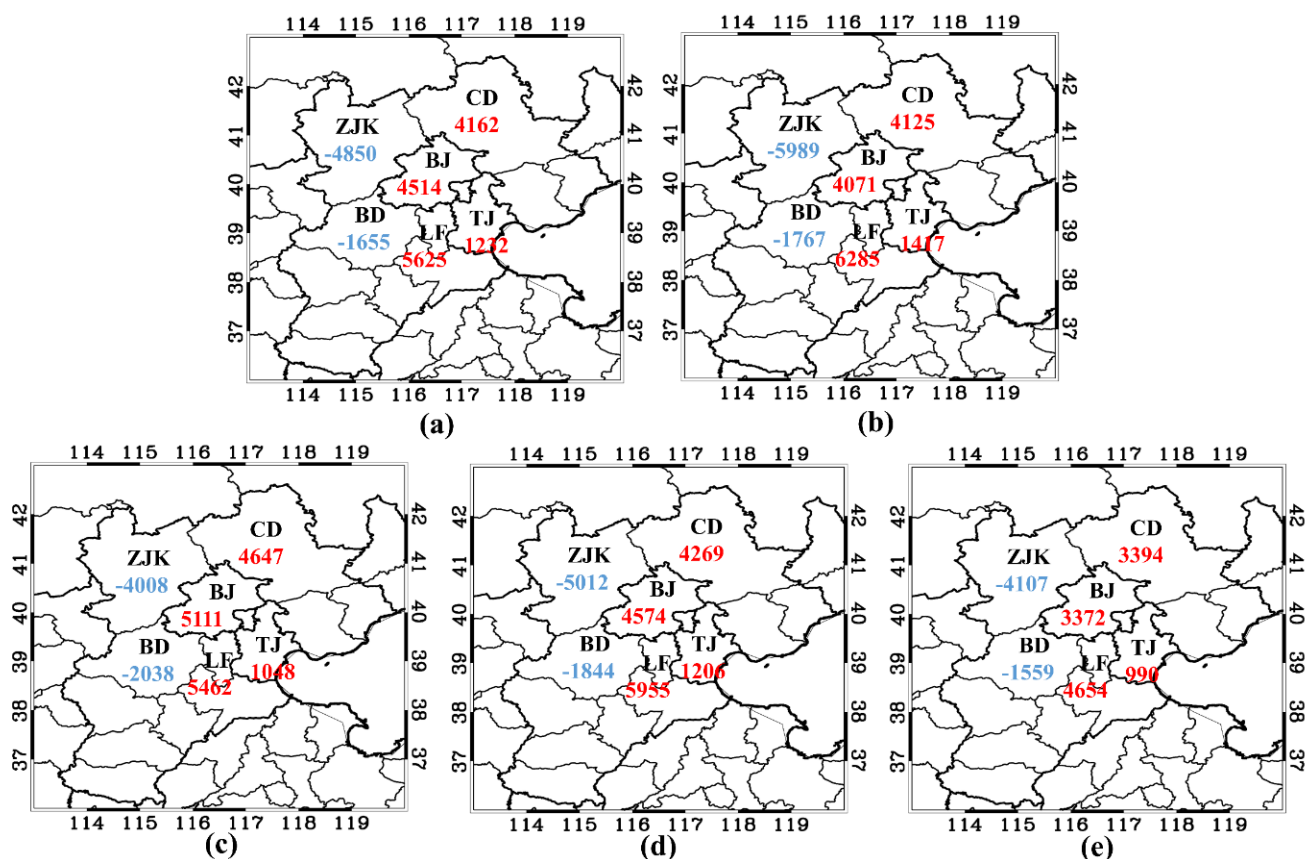


Figure 6. Four-month averaged tropospheric NO_x transport fluxes across city boundary for BJ. (a) Calculated NO₂ flux in W_2018 with MEIC-2017 inventory. (b) Same as (a) except with top-down W_2018 inventory. (c) Calculated NO₂ flux in W_2019 with MEIC-2017 inventory. (d) Same as (c) except with top-down W_2018 inventory. (e) Same as (c) except with top-down W_2019 inventory. Red number means net flux is inflow the NO_x. Blue number means net flux is outflow NO_x. Unit of flux is g/s.

Figure 7 displays the NO_x emissions and net fluxes of NO_x and NO_2 from W_2018 to W_2019. As illustrated in Figure 7a, compared with W_2018, BJ NO_x emissions remain unchanged (both use MEIC-2017), while NO_x input to BJ increased by 13.2% (increase of 597 g/s) due to unfavorable meteorological conditions. BJ total NO_x increment (including NO_x emissions and NO_x net flux) increased by 4.9% during W_2019. After the inventory adjustment, the top-down inventory demonstrates that, in W_2019, NO_x emissions and transport in BJ decreased by 20.4% (reduction of 1386 g/s) and 17.2% (reduction of 699 g/s), respectively. BJ total NO_x increment decreased by 19.2% compared to that of W_2018 (Figure 7b).

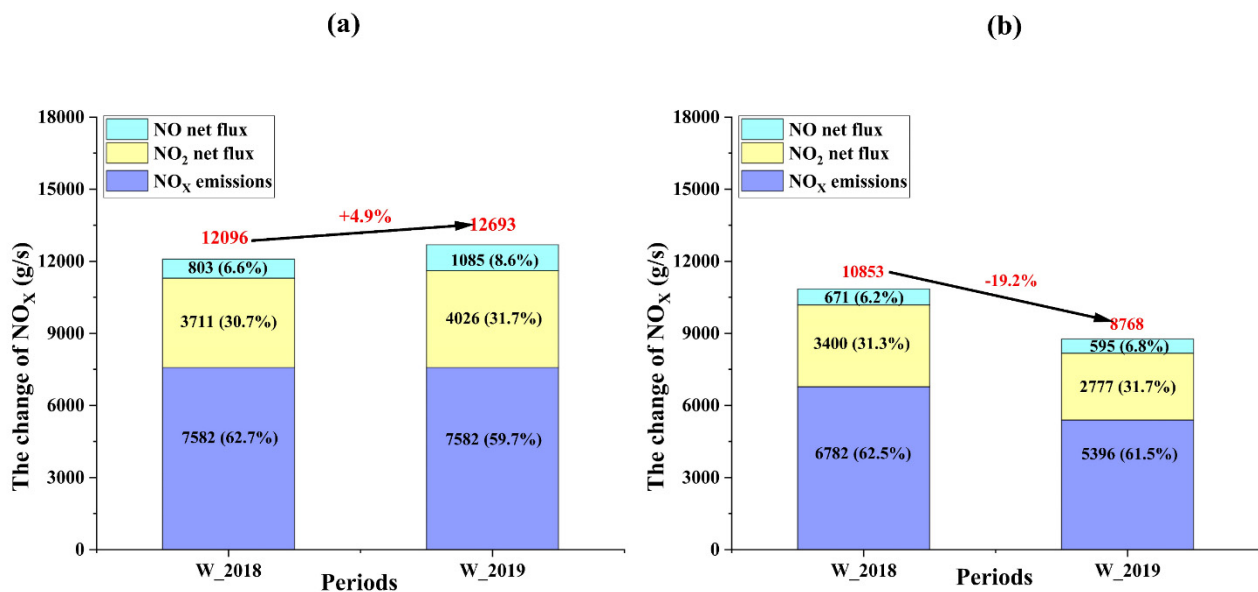


Figure 7. Variations in NO_x emissions, city boundary transport fluxes, and their relative contributions in BJ. (a) Simulated with MEIC-2017 inventory. (b) Simulated with top-down NO_x inventory.

In the two periods, BJ NO_x local emissions using MEIC-2017 were overestimated by 11.8% and 40.5%; and the NO_x transport flux was underestimated by 10.9% and 51.6%. Based on the top-down inventory, the proportions of emissions in the two winters were 62.5% and 61.5%, and the proportions of the city boundary transport fluxes were 37.5% and 38.5%.

4. Discussion

The assimilation of satellite observations in atmospheric chemical transport models is vital for improving the accuracy of air pollutant simulations. This study derived optimized NO_x emissions based on the TROPOMI/WRF-Chem relative difference using a mass balance approach. The pollutant distribution from TROPOMI is significantly impacted by meteorological conditions [66–68]. Thereby, the accuracy of this assimilated method (top-down emissions) decreases when strong transport on NO_2 occur. The Inversion errors and model-based simulation errors relating local NO_2 columns to local emissions constitute the uncertainty of top-down emissions. The overall error of the top-down emissions over NCP areas is estimated at ~50% [16].

Our results have taken COVID-19 lockdown and spring festival into account, which shows dramatic reductions (~50%) in NO_x emissions over January 2020. Our results comply with the literature, [69] indicated that concentrations of NO_2 decreased by ~45.1% observed by ground-based observations during January 2020 compared with that in January 2019. According to Figure 3, the slope of “Prior” is greater than 1, and the slope of TROPOMI Posterior is equal to 1. It means that the simulated NO_2 before assimilation is higher than the observation and more accurate after calibration.

Several studies have found that accurate representation of noonday NO₂ columns from highly localized sources requires a high model resolution. Since NO_x emissions show a strong variation on the 20 × 20 km² scale applied in this study. Increasing the model resolution can better represent these local gradients, thus improving the simulation of NO₂ concentrations [17,70,71].

The relative proportion of NO_x transport in BJ is about 40%. Similar results have been obtained in studies using a comparable regional model [65]. During the Asia-Pacific Economic Cooperation Forum week, non-local emissions contributed to 41.3% of the total PM_{2.5} concentration in BJ, emphasizing the correctness of strict and synergistic emissions control for BJ and its surrounding provinces.

Future work can be continued on the change of ozone and PM_{2.5} affected by the NO_x emission variety after TROPOMI assimilation.

5. Conclusions

By optimizing NO_x emissions with TROPOMI observations, sufficient NO₂ simulation performance can be achieved, and the mean relative error can be reduced by 45%. Cities with high NO_x emissions exhibit a pronounced decline (by 25–58%) after inventory adjustment. Particularly in January 2020, NO_x exhibited a reduction of approximately 50% in BTH compared with that in January 2019. For BJ, in W_2018 and W_2019, the bottom-up NO_x emissions were overestimated by 11.8% and 40.5% when compared to the top-down NO_x emissions, respectively. According to the top-down inventory, compared with those of W_2018, NO_x emissions in BJ decreased by 20.4% during W_2019. A city with decreased NO₂ concentration may be due to not only reduced NO_x emissions but also lower NO₂ inflows. We found that NO_x emissions can account for approximately 60% of the NO_x concentration, and the remaining 40% is caused by regional transport.

Moreover, by analyzing the regional horizontal transport flux, we can identify the major sources and the strengths of NO_x emissions without an immediately updated bottom-up inventory. This approach can be used to evaluate the effectiveness of implementing emission control measures, particularly during special events.

Transport fluxes depend on wind speed and emissions. This NO_x inflow and outflow fluxes can be calculated according to the city boundaries transport. In W_2018 and W_2019, the BJ NO_x input fluxes using MEIC-2017 were overestimated by 10.9% and 51.6%, respectively. The top-down inventory indicated the major NO_x input and output directions and their specific NO_x flux values for BJ, which were the NO_x inflows from ZJK and BD and outflows to CD, TJ, and LF during the wintertime. Compared with W_2018, the NO_x input flux decreased by 17.2% (−699 g/s) in BJ during W_2019, which resulted from negative meteorological conditions (+503 g/s) and positive NO_x emission controls (−1202 g/s). These results illustrate the effectiveness of reducing local emissions through emissions controls.

Supplementary Materials: Available at <https://www.mdpi.com/article/10.3390/rs13091798/s1>. Figure S1: Monthly NO_x emissions. (a–b) Taken from the MEIC-2017. (e–h) Top-down NO_x emissions derived from TROPOMI NO₂ VCDs in W_2018. (i–l) Same as (e–h) except in W_2019. Figure S2: Difference in surface NO_x emissions between MEIC-2017 and top-down NO_x emissions (a–h); (i–l) Change in surface NO_x emissions between top-down W_2018 and top-down W_2019. Figure S3: Monthly averaged tropospheric NO₂ VCDs simulated from MEIC-2017 (a–h) and top-down NO_x emissions (i–t). Note that, (a–d) and (i–l) using the same meteorological condition (W_2018), while the different NO_x inventories. (e–h) and (m–t) also using the same meteorological condition (W_2019), while the different NO_x inventories. Figure S4: Variation in monthly averaged tropospheric NO₂ VCDs simulated from MEIC-2017 and top-down NO_x emissions. Note that, (a–d) using the meteorological condition in W_2018, while (e–l) using the same meteorological condition (W_2019). Figure S5: Monthly tropospheric NO₂ regional transport flux drive from MEIC-2017 (a–h) and top-down NO_x emissions (i–t). Note that, (a–d) and (i–l) using the same meteorological condition (W_2018), while the different NO_x inventories. (e–h) and (m–t) also using the same meteorological condition (W_2019), while the different NO_x inventories. Figure S6: Variation in monthly averaged tropospheric NO₂ regional transport flux drive from MEIC-2017 and top-down NO_x emissions. Note

that, (a–d) using the meteorological condition in W_2018, while (e–l) using the same meteorological condition (W_2019).

Author Contributions: Conceptualization, Q.H., M.G., C.Z. (Chun Zhao) and C.L.; Data curation, Y.Z., C.Z. (Chengxin Zhang), L.Y. and X.H.; Formal analysis, Y.Z.; Funding acquisition, Q.H.; Investigation, Y.Z., T.L., Y.T. and W.S.; Methodology, Y.Z., M.G. and C.Z. (Chun Zhao); Project administration, Q.H. and C.L.; Resources, C.L.; Software, C.Z. (Chengxin Zhang), T.L. and W.S. All authors have read and agreed to the published version of the manuscript.

Funding: This research was supported by grants from the National Key Research and Development Program of China (No. 2017YFC0210002, 2018YFC0213104, 2016YFC0203302 and 2017YFC0212800), the National Natural Science Foundation of China (No. 41722501, 51778596, 41977184 and 41941011), Anhui Science and Technology Major Project (No. 18030801111), the Strategic Priority Research Program of the Chinese Academy of Sciences (No. XDA23020301), the National Key Project for Causes and Control of Heavy Air Pollution (No. DQGG0102 and DQGG0205), the Natural Science Foundation of Anhui Province (1908085QD170), Key Research and Development Project of Anhui Province (202004i07020002); the Youth Innovation Promotion Association of CAS (2021443); the Young Talent Project of the Center for Excellence in Regional Atmospheric Environment, CAS (CERAE202004).

Institutional Review Board Statement: Not applicable.

Informed Consent Statement: Not applicable.

Data Availability Statement: The WRF-Chem simulations output and TROPOMI product can be requested to the corresponding author.

Acknowledgments: We acknowledge all developers for contributing to the development of the WRF-Chem model, and are thankful for the use of the WRF-Chem preprocessor tool mozbc and fire_emiss provided by the Atmospheric Chemistry Observations and Modeling Lab (ACOM) of NCAR. We thank NCEP for providing final reanalysis dataset (FNL). We thank Zhang Qiang's team at Department of Earth System Science, Tsinghua University for providing the MEIC inventory. We thank the Copernicus Open Access Hub and the European Space Agency for making the Sentinel-5P Level 1 and Level 2 products available online (<https://scihub.copernicus.eu/>), last access: 15 March 2020). We thank National Climate Detector Center of NOAA for offering surface meteorological data available online.

Conflicts of Interest: The authors declare no conflict of interest.

Abbreviations

The following abbreviations are used in this manuscript:

"2 + 26" cities

BJ	Beijing
TJ	Tianjin
SJZ	Shijiazhuang
TS	Tangshan
BD	Baoding
LF	Langfang
CZ	Cangzhou
HS	Hengshui
HD	Handan
XT	Xingtai
TY	Taiyuan
YQ	Yangquan
ChangZ	Changzhi
JC	Jincheng
JN	Jinan
ZB	Zibo

LC	Liaocheng
DZ	Dezhou
BZ	Binzhou
JNing	Jining
HZ	Heze
ZZ	Zhengzhou
XX	Xinxiang
HB	Hebi
AY	Anyang
JZ	Jiaozuo
PY	Puyang
KF	Kaifeng
ZJK	Zhangjiakou
CD	Chengde
Another two neighboring cities in the north of Beijing	
ZJK	Zhangjiakou
CD	Chengde

References

- Vuuren, D.P.; Bouwman, L.F.; Smith, S.J.; Dentener, F. Global projections for anthropogenic reactive nitrogen emissions to the atmosphere: An assessment of scenarios in the scientific literature. *Curr. Opin. Environ. Sustain.* **2011**, *3*, 359–369. [[CrossRef](#)]
- Tanvir, A.; Javed, Z.; Jian, Z.; Zhang, S.; Bilal, M.; Xue, R.; Wang, S.; Bin, Z. Ground-Based MAX-DOAS observations of tropospheric NO₂ and HCHO during COVID-19 lockdown and spring festival over Shanghai, China. *Remote Sens.* **2021**, *13*, 488. [[CrossRef](#)]
- Jin, Y.; Andersson, H.; Zhang, S. Air pollution control policies in China: A retrospective and prospects. *Int. J. Environ. Res. Public Health* **2016**, *13*, 1219. [[CrossRef](#)]
- Tan, W.; Zhao, S.; Liu, C.; Chan, K.L.; Xie, Z.; Zhu, Y.; Su, W.; Zhang, C.; Liu, H.; Xing, C.; et al. Estimation of winter time NO_x emissions in Hefei, a typical inland city of China, using mobile MAX-DOAS observations. *Atmos. Environ.* **2019**, *200*, 228–242. [[CrossRef](#)]
- Vu, T.V.; Shi, Z.; Cheng, J.; Zhang, Q.; He, K.; Wang, S.; Harrison, R.M. Assessing the impact of clean air action on air quality trends in Beijing using a machine learning technique. *Atmos. Chem. Phys.* **2019**, *19*, 11303–11314. [[CrossRef](#)]
- Lu, K.; Guo, S.; Tan, Z.; Wang, H.; Shang, D.; Liu, Y.; Li, X.; Wu, Z.; Hu, M.; Zhang, Y. Exploring atmospheric free-radical chemistry in China: The self-cleansing capacity and the formation of secondary air pollution. *Natl. Sci. Rev.* **2019**, *6*, 579–594. [[CrossRef](#)]
- Tan, W.; Liu, C.; Wang, S.; Xing, C.; Su, W.; Zhang, C.; Xia, C.; Liu, H.; Cai, Z.; Liu, J. Tropospheric NO₂, SO₂, and HCHO over the East China Sea, using ship-based MAX-DOAS observations and comparison with OMI and OMPS satellite data. *Atmos. Chem. Phys.* **2018**, *18*, 15387–15402. [[CrossRef](#)]
- Goldberg, D.L.; Lu, Z.; Streets, D.G.; de Foy, B.; Griffin, D.; McLinden, C.A.; Lamsal, L.N.; Krotkov, N.A.; Eskes, H. Enhanced Capabilities of TROPOMI NO₂: Estimating NO_x from North American Cities and Power Plants. *Environ. Sci. Technol.* **2019**, *53*, 12594–12601. [[CrossRef](#)]
- Bucseles, E.J.; Krotkov, N.A.; Celarier, E.A.; Lamsal, L.N.; Swartz, W.H.; Bhartia, P.K.; Boersma, K.F.; Veefkind, J.P.; Gleason, J.F.; Pickering, K.E. A new stratospheric and tropospheric NO₂ retrieval algorithm for nadir-viewing satellite instruments: Applications to OMI. *Atmos. Meas. Tech.* **2013**, *6*, 2607–2626. [[CrossRef](#)]
- Georgoulias, A.K.; van der, A.R.J.; Stammes, P.; Boersma, K.F.; Eskes, H.J. Trends and trend reversal detection in 2 decades of tropospheric NO₂ satellite observations. *Atmos. Chem. Phys.* **2019**, *19*, 6269–6294. [[CrossRef](#)]
- Shah, V.; Jacob, D.J.; Li, K.; Silvern, R.F.; Zhai, S.; Liu, M.; Lin, J.; Zhang, Q. Effect of changing NO_x lifetime on the seasonality and long-term trends of satellite-observed tropospheric NO₂ columns over China. *Atmos. Chem. Phys.* **2020**, *20*, 1483–1495. [[CrossRef](#)]
- Yin, H.; Sun, Y.; Liu, C.; Zhang, L.; Lu, X.; Wang, W.; Shan, C.; Hu, Q.; Tian, Y.; Zhang, C.; et al. FTIR time series of stratospheric NO₂ over Hefei, China, and comparisons with OMI and GEOS-Chem model data. *Opt. Express.* **2019**, *27*, A1225–A1240. [[CrossRef](#)] [[PubMed](#)]
- Stavrou, T.; Müller, J.F.; Boersma, K.F.; De Smedt, I.; van der, A.R.J. Assessing the distribution and growth rates of NO_x emission sources by inverting a 10-year record of NO₂ satellite columns. *Geophys. Res. Lett.* **2008**, *35*. [[CrossRef](#)]
- Lorente, A.; Boersma, K.F.; Eskes, H.J.; Veefkind, J.P.; van Geffen, J.; de Zeeuw, M.B.; Denier van der Gon, H.A.C.; Beirle, S.; Krol, M.C. Quantification of nitrogen oxides emissions from build-up of pollution over Paris with TROPOMI. *Sci. Rep.* **2019**, *9*, 20033. [[CrossRef](#)]
- Kong, H.; Lin, J.; Zhang, R.; Liu, M.; Weng, H.; Ni, R.; Chen, L.; Wang, J.; Yan, Y.; Zhang, Q. High-resolution (0.05° × 0.05°) NO_x emissions in the Yangtze River Delta inferred from OMI. *Atmos. Chem. Phys.* **2019**, *19*, 12835–12856. [[CrossRef](#)]
- Zhao, C.; Wang, Y. Assimilated inversion of NO_x emissions over east Asia using OMI NO₂ column measurements. *Geophys. Res. Lett.* **2009**, *36*. [[CrossRef](#)]

17. Goldberg, D.L.; Saide, P.E.; Lamsal, L.N.; de Foy, B.; Lu, Z.; Woo, J.-H.; Kim, Y.; Kim, J.; Gao, M.; Carmichael, G.; et al. A top-down assessment using OMI NO₂ suggests an underestimate in the NO_x emissions inventory in Seoul, South Korea, during KORUS-AQ. *Atmos. Chem. Phys.* **2019**, *19*, 1801–1818. [[CrossRef](#)]
18. Vinken, G.C.M.; Boersma, K.F.; van Donkelaar, A.; Zhang, L. Constraints on ship NO_x emissions in Europe using GEOS-Chem and OMI satellite NO₂ observations. *Atmos. Chem. Phys.* **2014**, *14*, 1353–1369. [[CrossRef](#)]
19. Rasool, Q.Z.; Zhang, R.; Lash, B.; Cohan, D.S.; Cooter, E.J.; Bash, J.O.; Lamsal, L.N. Enhanced representation of soil NO emissions in the Community Multiscale Air Quality (CMAQ) model version 5.0.2. *Geosci. Model Dev.* **2016**, *9*, 3177–3197. [[CrossRef](#)]
20. Souri, A.H.; Choi, Y.; Jeon, W.; Li, X.; Pan, S.; Diao, L.; Westenbarger, D.A. Constraining NO_x emissions using satellite NO₂ measurements during 2013 DISCOVER-AQ Texas campaign. *Atmos. Environ.* **2016**, *131*, 371–381. [[CrossRef](#)]
21. Nault, B.A.; Laughner, J.L.; Wooldridge, P.J.; Crounse, J.D.; Dibb, J.; Diskin, G.; Peischl, J.; Podolske, J.R.; Pollack, I.B.; Ryerson, T.B.; et al. Lightning NO_x emissions: Reconciling measured and modeled estimates with updated NO_x chemistry. *Geophys. Res. Lett.* **2017**, *44*, 9479–9488. [[CrossRef](#)]
22. Zhou, D.; Ding, K.; Huang, X.; Liu, L.; Liu, Q.; Xu, Z.; Jiang, F.; Fu, C.; Ding, A. Transport, mixing and feedback of dust, biomass burning and anthropogenic pollutants in eastern Asia: A case study. *Atmos. Chem. Phys.* **2018**, *18*, 16345–16361. [[CrossRef](#)]
23. Zheng, G.J.; Duan, F.K.; Su, H.; Ma, Y.L.; Cheng, Y.; Zheng, B.; Zhang, Q.; Huang, T.; Kimoto, T.; Chang, D.; et al. Exploring the severe winter haze in Beijing: The impact of synoptic weather, regional transport and heterogeneous reactions. *Atmos. Chem. Phys.* **2015**, *15*, 2969–2983. [[CrossRef](#)]
24. Xue, L.; Ding, A.; Cooper, O.; Huang, X.; Wang, W.; Zhou, D.; Wu, Z.; McClure-Begley, A.; Petropavlovskikh, I.; Andreae, M.O.; et al. ENSO and Southeast Asian biomass burning modulate subtropical trans-Pacific ozone transport. *Natl. Sci. Rev.* **2020**. [[CrossRef](#)]
25. Chen, L.; Xing, J.; Mathur, R.; Liu, S.; Wang, S.; Hao, J. Quantification of the enhancement of PM_{2.5} concentration by the downward transport of ozone from the stratosphere. *Chemosphere* **2020**, *255*, 126907. [[CrossRef](#)] [[PubMed](#)]
26. Abdalmogith, S.S.; Harrison, R.M. The use of trajectory cluster analysis to examine the long-range transport of secondary inorganic aerosol in the UK. *Atmos. Environ.* **2005**, *39*, 6686–6695. [[CrossRef](#)]
27. Li, D.; Liu, J.; Zhang, J.; Gui, H.; Du, P.; Yu, T.; Wang, J.; Lu, Y.; Liu, W.; Cheng, Y. Identification of long-range transport pathways and potential sources of PM_{2.5} and PM₁₀ in Beijing from 2014 to 2015. *J. Env. Sci.* **2017**, *56*, 214–229. [[CrossRef](#)] [[PubMed](#)]
28. Hong, Q.; Liu, C.; Chan, K.L.; Hu, Q.; Xie, Z.; Liu, H.; Si, F.; Liu, J. Ship-based MAX-DOAS measurements of tropospheric NO₂, SO₂, and HCHO distribution along the Yangtze River. *Atmos. Chem. Phys.* **2018**, *18*, 5931–5951. [[CrossRef](#)]
29. Sun, Y.; Chen, C.; Zhang, Y.; Xu, W.; Zhou, L.; Cheng, X.; Zheng, H.; Ji, D.; Li, J.; Tang, X. Rapid formation and evolution of an extreme haze episode in Northern China during winter 2015. *Sci. Rep.* **2016**, *6*, 1–9.
30. Qingqing, Z.; Xuhui, C.; Mengting, G.; Yu, S.; Xiaoling, Z. Long-term mean footprint and its relationship to heavy air pollution episodes in Beijing. *Acta Entiarum Nat. Univ. Pekin.* **2018**.
31. Yao, L.; Yang, L.; Yuan, Q.; Yan, C.; Dong, C.; Meng, C.; Sui, X.; Yang, F.; Lu, Y.; Wang, W. Sources apportionment of PM_{2.5} in a background site in the North China Plain. *Sci. Total Environ.* **2016**, *541*, 590–598. [[CrossRef](#)] [[PubMed](#)]
32. Wang, L.; Li, W.; Sun, Y.; Tao, M.; Xin, J.; Song, T.; Li, X.; Zhang, N.; Ying, K.; Wang, Y. PM_{2.5} Characteristics and regional transport contribution in five cities in southern north China plain, during 2013–2015. *Atmosphere* **2018**, *9*, 157. [[CrossRef](#)]
33. Zong, Z.; Wang, X.; Tian, C.; Chen, Y.; Fu, S.; Qu, L.; Ji, L.; Li, J.; Zhang, G. PMF and PSCF based source apportionment of PM_{2.5} at a regional background site in North China. *Atmos. Res.* **2018**, *203*, 207–215. [[CrossRef](#)]
34. Xing, C.; Liu, C.; Wang, S.; Chan, K.L.; Gao, Y.; Huang, X.; Su, W.; Zhang, C.; Dong, Y.; Fan, G.; et al. Observations of the vertical distributions of summertime atmospheric pollutants and the corresponding ozone production in Shanghai, China. *Atmos. Chem. Phys.* **2017**, *17*, 14275–14289. [[CrossRef](#)]
35. Chang, X.; Wang, S.; Zhao, B.; Cai, S.; Hao, J. Assessment of inter-city transport of particulate matter in the Beijing–Tianjin–Hebei region. *Atmos. Chem. Phys.* **2018**, *18*, 4843–4858. [[CrossRef](#)]
36. Dong, Z.; Wang, S.; Xing, J.; Chang, X.; Ding, D.; Zheng, H. Regional transport in Beijing-Tianjin-Hebei region and its changes during 2014–2017: The impacts of meteorology and emission reduction. *Sci. Total Environ.* **2020**, *737*, 139792. [[CrossRef](#)] [[PubMed](#)]
37. Ding, D.; Xing, J.; Wang, S.; Chang, X.; Hao, J. Impacts of emissions and meteorological changes on China’s ozone pollution in the warm seasons of 2013 and 2017. *Front. Environ. Sci. Eng.* **2019**, *13*, 1–9. [[CrossRef](#)]
38. Tie, X.; Brasseur, G.; Ying, Z. Impact of model resolution on chemical ozone formation in Mexico City: Application of the WRF-Chem model. *Atmos. Chem. Phys.* **2010**, *10*, 8983–8995. [[CrossRef](#)]
39. Grell, G.A.; Peckham, S.E.; Schmitz, R.; McKeen, S.A.; Frost, G.; Skamarock, W.C.; Eder, B. Fully coupled “online” chemistry within the WRF model. *Atmos. Environ.* **2005**, *39*, 6957–6975. [[CrossRef](#)]
40. Liu, H.; Liu, C.; Xie, Z.; Li, Y.; Huang, X.; Wang, S.; Xu, J.; Xie, P. A paradox for air pollution controlling in China revealed by “APEC Blue” and “Parade Blue”. *Sci. Rep.* **2016**, *6*, 34408. [[CrossRef](#)]
41. Li, M.; Liu, H.; Geng, G.; Hong, C.; Liu, F.; Song, Y.; Tong, D.; Zheng, B.; Cui, H.; Man, H.; et al. Anthropogenic emission inventories in China: A review. *Natl. Sci. Rev.* **2017**, *4*, 834–866. [[CrossRef](#)]
42. Zheng, B.; Tong, D.; Li, M.; Liu, F.; Hong, C.; Geng, G.; Li, H.; Li, X.; Peng, L.; Qi, J.; et al. Trends in China’s anthropogenic emissions since 2010 as the consequence of clean air actions. *Atmos. Chem. Phys.* **2018**, *18*, 14095–14111. [[CrossRef](#)]
43. Shu-Hua Chen, W.-Y.S. A one-dimensional time dependent cloud model. *J. Meteorol. Soc. Jpn.* **2002**, *80*, 99–118. [[CrossRef](#)]

44. Iacono, M.J.; Delamere, J.S.; Mlawer, E.J.; Shephard, M.W.; Clough, S.A.; Collins, W.D. Radiative forcing by long-lived greenhouse gases: Calculations with the AER radiative transfer models. *J. Geophys. Res.* **2008**, *113*. [[CrossRef](#)]
45. Grell, G.A.; Freitas, S.R. A scale and aerosol aware stochastic convective parameterization for weather and air quality modeling. *Atmos. Chem. Phys.* **2014**, *13*, 23845–23893. [[CrossRef](#)]
46. Tewari, M.; Chen, F.; Wang, W.; Dudhia, J.; LeMone, M.A.; Mitchell, K.M.; Ek, G.; Gayno, J.; Wegiel, R.; Cuenca, H. Implementation and verification of the unified NOAA land surface model in the WRF model. *Geoscience* **2004**.
47. Hong, S.Y.; Yign, N.; Jimy, D. A new vertical diffusion package with an explicit treatment of entrainment processes. *Mon. Weather Rev.* **2006**, *134*, 2318–2341. [[CrossRef](#)]
48. Zhang, C.; Liu, C.; Chan, K.L.; Hu, Q.; Liu, H.; Li, B.; Xing, C.; Tan, W.; Zhou, H.; Si, F.; et al. First observation of tropospheric nitrogen dioxide from the Environmental Trace Gases Monitoring Instrument onboard the GaoFen-5 satellite. *Light Sci. Appl.* **2020**, *9*, 1–9. [[CrossRef](#)] [[PubMed](#)]
49. Cugny, B.; Karafolas, N.; Armandillo, E.; van der Valk, N.; Lobb, D.; de Vries, J.; Veefkind, P.; Aben, I.; Wood, T.; Bhatti, I.S.; et al. TROPOMI, the Sentinel 5 precursor instrument for air quality and climate observations: Status of the current design. In *International Conference on Space Optics—ICSO 2012*; International Society for Optics and Photonics: Bellingham, Washington, DC, USA, 2017; Volume 10546, p. 105641Q. [[CrossRef](#)]
50. Su, W.; Liu, C.; Hu, Q.; Fan, G.; Xie, Z.; Huang, X.; Zhang, T.; Chen, Z.; Dong, Y.; Ji, X.; et al. Characterization of ozone in the lower troposphere during the 2016 G20 conference in Hangzhou. *Sci. Rep.* **2017**, *7*, 17368. [[CrossRef](#)]
51. Fayt, C.; De Smedt, I.; Letocart, V.; Merlaud, A.; Pinardi, G.; Van Roozendaal, M.; Roozendaal, M. QDOAS Software user manual. *Belg. Inst. Space Aeron. Bruss. Belg.* **2011**, *1*, 1–117.
52. Zara, M.; Boersma, K.F.; De Smedt, I.; Richter, A.; Peters, E.; van Geffen, J.H.G.M.; Beirle, S.; Wagner, T.; Van Roozendaal, M.; Marchenko, S.; et al. Improved slant column density retrieval of nitrogen dioxide and formaldehyde for OMI and GOME-2A from QA4ECV: Intercomparison, uncertainty characterisation, and trends. *Atmos. Meas. Tech.* **2018**, *11*, 4033–4058. [[CrossRef](#)]
53. Spurr, R.J.D. VLIDORT: A linearized pseudo-spherical vector discrete ordinate radiative transfer code for forward model and retrieval studies in multilayer multiple scattering media. *J. Quant. Spectrosc. Radiat. Transf.* **2006**, *102*, 316–342. [[CrossRef](#)]
54. Veefkind, J.P.; de Haan, J.F.; Sneep, M.; Levelt, P.F. Improvements to the OMI O₂–O₂ operational cloud algorithm and comparisons with ground-based radar-lidar observations. *Atmos. Meas. Tech.* **2016**, *9*, 6035–6049. [[CrossRef](#)]
55. Beirle, S.; Hormann, C.; Jockel, P.; Liu, S.; de Vries, M.P.; Pozzer, A.; Sihler, H.; Valks, P.; Wagner, T. The stratospheric estimation algorithm from Mainz (STREAM): Estimating stratospheric NO₂ from nadir-viewing satellites by weighted convolution. *Atmos. Meas. Tech.* **2016**, *9*, 2753–2779. [[CrossRef](#)]
56. Zhang, C.; Liu, C.; Hu, Q.; Cai, Z.; Su, W.; Xia, C.; Zhu, Y.; Wang, S.; Liu, J. Satellite UV-Vis spectroscopy: Implications for air quality trends and their driving forces in China during 2005–2017. *Light Sci. Appl.* **2019**, *8*, 1–12. [[CrossRef](#)] [[PubMed](#)]
57. Kuhlmann, G.; Hartl, A.; Cheung, H.M.; Lam, Y.F.; Wenig, M.O. A novel gridding algorithm to create regional trace gas maps from satellite observations. *Atmos. Meas. Tech.* **2014**, *7*, 451–467. [[CrossRef](#)]
58. Su, W.; Liu, C.; Chan, K.L.; Hu, Q.; Liu, H.; Ji, X.; Zhu, Y.; Liu, T.; Zhang, C.; Chen, Y.; et al. An improved TROPOMI tropospheric HCHO retrieval over China. *Atmos. Meas. Tech.* **2020**, *13*, 6271–6292. [[CrossRef](#)]
59. Walker, T.W.; Martin, R.V.; van Donkelaar, A.; Leaitch, W.R.; MacDonald, A.M.; Anlauf, K.G.; Cohen, R.C.; Bertram, T.H.; Huey, L.G.; Avery, M.A.; et al. Trans-Pacific transport of reactive nitrogen and ozone to Canada during spring. *Atmos. Chem. Phys.* **2010**, *10*, 8353–8372. [[CrossRef](#)]
60. Lamsal, L.N.; Martin, R.V.; Padmanabhan, A.; van Donkelaar, A.; Zhang, Q.; Sioris, C.E.; Chance, K.; Kurosu, T.P.; Newchurch, M.J. Application of satellite observations for timely updates to global anthropogenic NO_x emission inventories. *Geophys. Res. Lett.* **2011**, *38*, 1–5. [[CrossRef](#)]
61. Visser, A.J.; Boersma, K.F.; Ganzeveld, L.N.; Krol, M.C. European NO_x emissions in WRF-Chem derived from OMI: Impacts on summertime surface ozone. *Atmos. Chem. Phys.* **2019**, *19*, 11821–11841. [[CrossRef](#)]
62. Jiang, F.; Wang, T.; Wang, T.; Xie, M.; Zhao, H. Numerical modeling of a continuous photochemical pollution episode in Hong Kong using WRF-chem. *Atmos. Environ.* **2008**, *42*, 8717–8727. [[CrossRef](#)]
63. Feng, T.; Zhou, W.; Wu, S.; Niu, Z.; Cheng, P.; Xiong, X.; Li, G. High-resolution simulation of wintertime fossil fuel CO₂ in Beijing, China: Characteristics, sources, and regional transport. *Atmos. Environ.* **2019**, *198*, 226–235. [[CrossRef](#)]
64. Miao, Y.; Guo, J.; Liu, S.; Liu, H.; Zhang, G.; Yan, Y.; He, J. Relay transport of aerosols to Beijing-Tianjin-Hebei region by multi-scale atmospheric circulations. *Atmos. Environ.* **2017**, *165*, 35–45. [[CrossRef](#)]
65. Gao, M.; Liu, Z.; Wang, Y.; Lu, X.; Ji, D.; Wang, L.; Li, M.; Wang, Z.; Zhang, Q.; Carmichael, G.R. Distinguishing the roles of meteorology, emission control measures, regional transport, and co-benefits of reduced aerosol feedbacks in “APEC Blue”. *Atmos. Environ.* **2017**, *167*, 476–486. [[CrossRef](#)]
66. Qu, Y.; Voulgarakis, A.; Wang, T.; Kasoar, M.; Wells, C.; Yuan, C.; Varma, S.; Mansfield, L. A study of the effect of aerosols on surface ozone through meteorology feedbacks over China. *Atmos. Chem. Phys.* **2021**, *21*, 5705–5718. [[CrossRef](#)]
67. Wang, Z.; Uno, I.; Yumimoto, K.; Itahashi, S.; Chen, X.; Yang, W.; Wang, Z. Impacts of COVID-19 lockdown, Spring Festival and meteorology on the NO₂ variations in early 2020 over China based on in-situ observations, satellite retrievals and model simulations. *Atmos. Environ.* **2021**, *244*, 117972. [[CrossRef](#)]

-
68. Zhai, S.; Jacob, D.J.; Wang, X.; Shen, L.; Li, K.; Zhang, Y.; Gui, K.; Zhao, T.; Liao, H. Fine particulate matter (PM_{2.5}) trends in China, 2013–2018: Separating contributions from anthropogenic emissions and meteorology. *Atmos. Chem. Phys.* **2019**, *19*, 11031–11041. [[CrossRef](#)]
 69. Li, L.; Li, Q.; Huang, L.; Wang, Q.; Zhu, A.; Xu, J.; Liu, Z.; Shi, L.; Li, R.; Azari, M.; et al. Air quality changes during the COVID-19 lockdown over the Yangtze River Delta Region: An insight into the impact of human activity pattern changes on air pollution variation. *Sci. Total Environ.* **2020**, *732*, 139282. [[CrossRef](#)]
 70. Salmon, O.E.; Shepson, P.B.; Ren, X.; He, H.; Hall, D.L.; Dickerson, R.R.; Stirm, B.H.; Brown, S.S.; Fibiger, D.L.; McDuffie, E.E.; et al. Top-Down estimates of NO_x and CO emissions from Washington, D.C.-Baltimore during the winter campaign. *J. Geophys. Res. Atmos.* **2018**. [[CrossRef](#)]
 71. Hu, X.-M.; Nielsen-Gammon, J.W.; Zhang, F. Evaluation of three planetary boundary layer schemes in the WRF model. *J. Appl. Meteorol. Climatol.* **2010**, *49*, 1831–1844. [[CrossRef](#)]